A&A 497, 805–813 (2009)
DOI: 10.1051/0004-6361/200811181
© ESO 2009

Astronomy & Astrophysics

Properties of the ionised plasma in the vicinity of the neutron-star X-ray binary EXO 0748–676

J. C. A. van Peet[1], E. Costantini[1], M. Méndez[2], F. B. S. Paerels[3], and J. Cottam[4]

[1] SRON, Netherlands Institute for Space Research, Sorbonnelaan 2, 3584 CA Utrecht, The Netherlands
e-mail: e.costantini@sron.nl
[2] Kapteyn Astronomical Institute University of Groningen Postbus 800 9700 AV Groningen, The Netherlands
[3] Columbia Astrophysics Laboratory, Department of Astronomy, Columbia University, 550 West 120th Street, New York, NY 10027, USA
[4] Exploration of the universe Division, Code 660, NASA/GSFC, Greenbelt, MD 20771, USA

Received 17 October 2008 / Accepted 17 February 2009

ABSTRACT

Aims. We present the spectral analysis of a large set of XMM-*Newton* observations of EXO 0748–676, a bright dipping low-mass X-ray binary. In particular, we focus on the dipping phenomenon as a result of changes in the properties of the ionised gas close to the source.

Methods. We analysed the high-resolution spectra collected with the reflection grating spectrometer on board *XMM-Newton*. We studied dipping and persistent spectra separately. We used the Epic data to constrain the broad-band continuum. We explored two simple geometrical scenarios for which we derived physical quantities of the absorbing material like the density, size, and mass.

Results. We find that the continuum is absorbed by a neutral gas, and by both a collisionally (temperature $T \sim 70$ eV) and photoionised (ionisation parameter $\log \xi \sim 2.5$) absorbers. Emission lines from OVII and OVIII are also detected. This is the first time that evidence of a collisionally ionised absorber has been found in a low-mass X-ray binary. The collisionally ionised absorber may be in the form of dense ($n > 10^{14}$ cm^{-3}) filaments, located at a distance $r \gtrsim 10^{11}$ cm. During dips, the photoionised absorber significantly increases its column density (factor 2–4) while becoming less ionised. This strengthens the idea that the colder material of the accretion stream impinging the disc is passing on our line of sight during dips. In this scenario, we find that the distance from the neutron star to the impact region ($\sim 5 \times 10^{10}$ cm) is similar to the size of the neutron star's Roche lobe. The gas observed during the persistent state may have a flattened geometry. Finally, we explore the possibility of the existence of material forming an initial, hotter portion of a circumbinary disc.

Key words. atomic processes – stars: binaries: general – X-rays: binaries – X-rays: individuals: EXO 0748–676

1. Introduction

Low-mass X-ray binaries (LMXB) show different types of variability in their light curve, including X-ray bursts, eclipses, and characteristic obscuring events called dips. A dip shows up in the light curve as a decrease in count-rate, which can be as deep as an eclipse, but with a much less clear start and end. Dips are probably caused by the line of sight intercepting the impact region of the accretion stream on the accretion disc (White & Swank 1982), and are therefore seen in systems with inclinations in the range of 60°–80° (Frank et al. 1987).

Two different models have been used to explain the dipping emission. In the first model (e.g. Parmar et al. 1986) two components (both power laws with an exponential cut off) are used to model the dipping emission. The first component is absorbed and the second one is not. This approach is sometimes referred to as the "absorbed + unabsorbed approach".

The second model, which consists of two types of emitting components, was proposed by Church et al. (1998). The first component is point-like blackbody emission from the neutron star itself, and the second component is extended Comptonised emission from the accretion disc corona. During dipping intervals, the accretion disc corona is progressively covered, hence the name "progressive covering approach".

Recently, Boirin et al. (2005) have proposed a different approach to modelling the dipping spectra in the LMXB 4U 1323–62. They find that the spectral changes during dipping emission can be modelled by varying the properties of a photoionised absorber (i.e. column density and ionisation parameter). No absorbed + unabsorbed components or progressive and partial covering of an extended corona is necessary and absorption lines and the continuum are modelled self consistently. Díaz Trigo et al. (2006) show that this approach can be used on a number of other X-ray binaries exhibiting dipping behaviour, among which also EXO 0748–676.

EXO 0748–676 is an LMXB that shows all the variability mentioned above: bursts, eclipses, and dips. It was discovered in 1986 (Parmar et al. 1986; Gottwald et al. 1986) and has been studied regularly since its discovery (Parmar et al. 1991; Hertz et al. 1995, 1997; Thomas et al. 1997; Church et al. 1998; Sidoli et al. 2005; Wolff et al. 2005) especially since the launch of the high resolution X-ray observatories XMM-*Newton* (Bonnet-Bidaud et al. 2001; Cottam et al. 2001, 2002; Homan et al. 2003; Díaz Trigo et al. 2006), and *Chandra* (Jimenez-Garate et al. 2003).

Parmar et al. (1986) derived the basic properties for EXO 0748–676. The LMXB has a period of 3.82 h as measured by X-ray eclipse timings, and the eclipses themselves have a duration of 8.3 min. Assuming a compact object of 1.4 $M_\odot$,

Table 1. XMM observation summary for EXO 0748–676.

Orbit	Obs. ID	Instruments	Obs. date (yymmdd)	observing time (ks) total	per	dip	Group	Spectrum mos/pn
0055	0122310301	mos/rgs	00-03-28	61.0	11.9	0.9	A	–
0067	0123500101	mos/pn/rgs	00-04-21	62.1	16.9	14.5	A	yes
0212	0134561101	mos/pn/rgs	01-02-03	8.4	0.0	3.8	A	–
0212	0134561201	mos/pn/rgs	01-02-04	6.6	0.3	1.7	A	–
0212	0134561301	mos/pn/rgs	01-02-04	6.9	1.6	1.3	A	–
0212	0134561401	mos/pn/rgs	01-02-04	6.6	1.5	1.4	A	–
0212	0134561501	mos/pn/rgs	01-02-04	6.6	1.2	1.3	A	–
0338	0134562101	mos/rgs	01-10-13	8.7	4.7	2.1	B	–
0338	0134562201	mos/rgs	01-10-13	6.9	4.8	1.3	B	–
0338	0134562301	mos/rgs	01-10-13	6.9	6.2	0.0	B	–
0338	0134562401	mos/rgs	01-10-13	6.9	2.8	2.3	B	–
0338	0134562501	mos/rgs	01-10-13/14	6.9	2.5	2.4	B	yes
0693	0160760201	mos/pn/rgs	03-09-21/22	93.4	41.5	23.1	C2	–
0694	0160760301	mos/pn/rgs	03-09-23/24	108.3	47.8	29.6	C3	yes
0695	0160760401	mos/pn/rgs	03-09-25/26	82.0	29.4	26.6	C3	–
0710	0160760801	mos/pn/rgs	03-10-25/26	67.9	21.8	18.1	C1	yes
0719	0160761301	mos/pn/rgs	03-11-12/13	94.7	31.3	35.3	C2	yes

Parmar et al. (1986) infer the mass of the companion to be between 0.085 $M_\odot$ and 0.45 $M_\odot$ and the system inclination between 75° and 82°. Recently a strong X-ray burst was observed (Wolff et al. 2005) from which a distance to EXO 0748–676 was derived that depends on whether the burst is hydrogen dominated (5.9 ± 0.9 kpc) or helium dominated (7.7 ± 0.9 kpc). In this paper we use the average value of 6.8 kpc.

We study here the ionisation state of the accretion disc around the neutron star of EXO 0748–676 in order to get a better understanding of the geometry, dynamics and ion stratification of the disc. We use all RGS data available in the wavelength range 7–35 Å.

In Sect. 2 we describe the observations and the data analysis, in Sect. 3 we present the results of the spectral fitting. In Sect. 4 we discuss the results and derive physical parameters of the system and in Sect. 5 we present our conclusions.

2. Data analysis

The data were taken from the XMM-*Newton* archives and were acquired with the Epic PN (Strüder et al. 2001), Epic MOS (Turner et al. 2001) and RGS (den Herder et al. 2001) instruments. For the analysis of each data set we require first the availability of the RGS and then of either the PN or MOS cameras (Table 1). We processed the data with version 6.5.0 of the XMM-*Newton* Science Analysis System (SAS). For the Epic analysis, the background was extracted from a circular region in the same field of view of the source. From this region we produce a light curve from which we removed any background flares. Only four observations were totally discarded because of a persistently flaring background. To obtain the source light curve and spectrum we use an annular extraction region ($R_{\rm in} \approx 8''$ and $R_{\rm out} \approx 51.5''$) to prevent pile-up. We divide the source radiation into hard ($5 \leq E(\rm keV) \leq 10$) and soft ($0.3 \leq E(\rm keV) \leq 5$) X-ray emission. We use the hard X-ray light curve to obtain the starting and ending times for the bursts and the eclipses, since this energy range is marginally affected by dipping (Díaz Trigo et al. 2006). EXO 0748–676 occasionally shows two, or even three, bursts in a row (Boirin et al. 2007), with an inter-burst time that is much shorter than between two normal bursts. We count these double and triple bursts as one, since we are only interested in the starting and ending times of the total interval containing bursts.

We also use the PN data to obtain the Good Time Intervals (GTI) for the dipping and eclipsing emission (we will call persistent emission everything that is not dip, burst or eclipse). These GTIs were subsequently used to extract the RGS spectra. If, for a certain observation, PN (or MOS) were not switched on at the same time as RGS, we only use the overlapping intervals.

Next, we divide the hard X-ray light curve by the soft X-ray light curve. We use the resulting hardness ratio curve to distinguish between dipping and persistent emission: a dip interval shows up as an increase in the hardness ratio. We use the average of a representative portion of the hardness ratio curve that clearly belongs to the persistent emission to select dipping and persistent emission: values higher than 2 times the average persistent hardness ratio were selected as dipping emission.

Upon close inspection of the hardness ratio curves we found that it was not possible to distinguish between persistent and dipping emission in the way that was described above for the observations from orbits 0692 and 0708. The reason for this is that the hardness ratio curve for these observations does not show clear separate periods of dipping and persistent emission as compared to a normal case. For this reason, even if these two data sets satisfied our first selection criteria, we did not analyse them any further.

We process the RGS data with the SAS task "rgsproc". After we check the source coordinates and correct them if necessary, we create a spectrum of the RGS.

We apply an effective area correction to the RGS data processed with SAS version 6.5.0 (private communication of Vink)[1]. We fit the area-corrected spectra with the X-ray and UV fitting package SPEX[2] (Kaastra et al. 1996). The best fit was found by minimisation of the χ^2. Errors are at 1σ unless otherwise stated.

2.1. The data set

In Table 1 we list the observations from the XMM-*Newton* archive used in this paper. In the first column the orbit in which

[1] More information can be found on the website of the XMM-*Newton* users group: http://xmm.vilspa.esa.es/external/xmm_user_support/usersgroup/20060518/rgs_calib_eff.pdf). This correction has been incorporated into subsequent SAS releases.

[2] http://www.sron.nl/divisions/hea/spex/

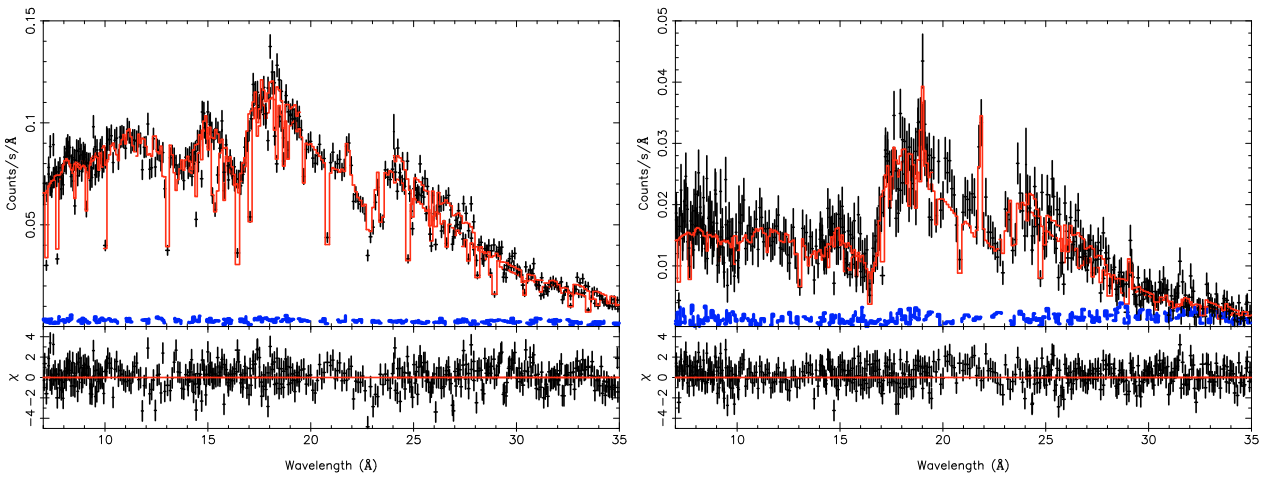

Fig. 1. Two representative spectra of RGS1 and RGS2, taken from obsid 0160760201. *The left plot* shows the persistent spectrum and *the right plot* shows the dipping spectrum. In both plots *the upper panel* shows the data (points) and model (solid line) in counts s^{-1} $Å^{-1}$. The dotted line at the bottom is the background. *The lower panel* shows the model residuals ((data-model)/error). The data have been rebinned for clarity.

the observation was made is listed. The second column shows the observation identifier and the third column shows which instruments were used to observe the source. The "obs. date" column gives the date on which the observation was made. The label "observing time" gives the time subdivided in "total", persistent ("per") and dipping ("dip") times. Differences are caused mainly by the fact that eclipses and bursts are left out.

We grouped the observations, when possible, (column "group" in Table 1) using the SAS-task "rgscombine". The first criterion for combining separate spectra is to look whether the observations were close in time. Secondly, we fit a continuum model including absorption (as defined in the next sections) to the data and calculate the errors of the model parameters. If the parameters of the separate observations are consistent within the errors, we combine the observations.

We combine the observations from orbits 0055, 0067 and 0212 into group A, the observations from orbit 0338 into group B and the observations from orbits 06XX/07XX in three groups. In particular, we kept the observation from orbit 0710 as a separate group C1. We then combined the observations from orbits 0693 and 0719 into group C2, those from orbits 0694 and 0695 into group C3 (Table 1).

We use a single observation from each of the groups defined in Table 1 to create a spectrum of the PN (or MOS, if no PN is present) data and we fit both the RGS spectra and the PN spectrum of a group simultaneously to obtain the best fit. The observation we use to obtain the PN spectra is indicated in the last column of Table 1. There are two reasons to use PN data. The first is to constrain the power-law photon index in the wavelength range of the RGS instrument. The second is that PN data may offer us further constrains on a possible highly ionised absorber, whose features would show up in the 6–7 keV band (e.g. Boirin et al. 2005).

2.2. Spectral modelling

Two representative RGS spectra of persistent and dipping emission are plotted in Fig. 1. In both spectra we see a number of interesting absorption features. At 23.1 Å we see an absorption edge that is produced by neutral oxygen in the interstellar medium. We also see two other absorption edges, at 14.2 Å and 16.8 Å due to OVIII and OVII respectively. We can also clearly discern two emission lines, OVII at 21.8 Å and OVIII at 19 Å, the latter being more evident in the dipping spectrum.

As a starting point, we modelled the RGS spectra following Díaz Trigo et al. (2006), who analysed the lower resolution data of Epic-PN (orbit 0719). In particular their absorption model consisted of the combination of a neutral absorber and one photoionised absorber. The continuum was modelled by an emission from a black body and a powerlaw. In our case, applying the same model to the RGS wavelength range of 7–35 Å does not yield a satisfactory fit. In particular, the model is not capable of fitting the OVII and OVIII edges simultaneously, strongly suggesting the presence of a second, ionised, absorbing component.

We therefore departed from this starting model to fit the high-quality, high-resolution RGS data. For clarity, in the following the modelling is referred to the data set shown in Fig. 1 (left panel). In addition to the neutral absorber and one ionised absorber (with $\log\xi \sim 2.5$, where ξ is defined as the ratio between the ionising luminosity and the product between the gas density and its squared distance from the central source: $\xi = L/nr^2$) we included first an additional photoionised absorber (model *xabs* in SPEX). This did not yield a satisfactory fit (χ^2/d.o.f. = 2276.31/1188 = 1.92, for the persistent emission data. The column density of this additional component is $\sim 1.8 \times 10^{21}$ cm^{-2} with ionisation parameter $\log\xi \sim 0.8$. The OVII edge region, close to the iron unresolved transition array (UTA), between 14 and 20 Å, is where the model fails the most in fitting the data (Fig. 2). Next we tried a more complex absorption model, which mimics a continuous distribution of column densities as a function of the ionisation parameter (model *warm* in SPEX). The *warm* model did not improve the fit significantly with respect to a single-ionisation-parameter gas component.

The best fit is reached when a collisionally ionised gas component is added to the model (model *hot* in SPEX) with a χ^2/d.o.f. = 1631/1188 = 1.37 for this specific data set. The gas temperature is ~75 eV and the gas column density is $\sim 1.5 \times 10^{21}$ cm^{-2}. In Fig. 2 we compare the two interpretations in the 14–20 Å region where the OVII edge and the iron UTA creates a broad trough in the data. In the upper panel the transmission due to the photoionised (light line) and the collisionally ionised gas (dark line) are shown. In the next panel the data and the models, convolved by the instrument resolution, are shown (with the same colour labelling as above). It is evident that the

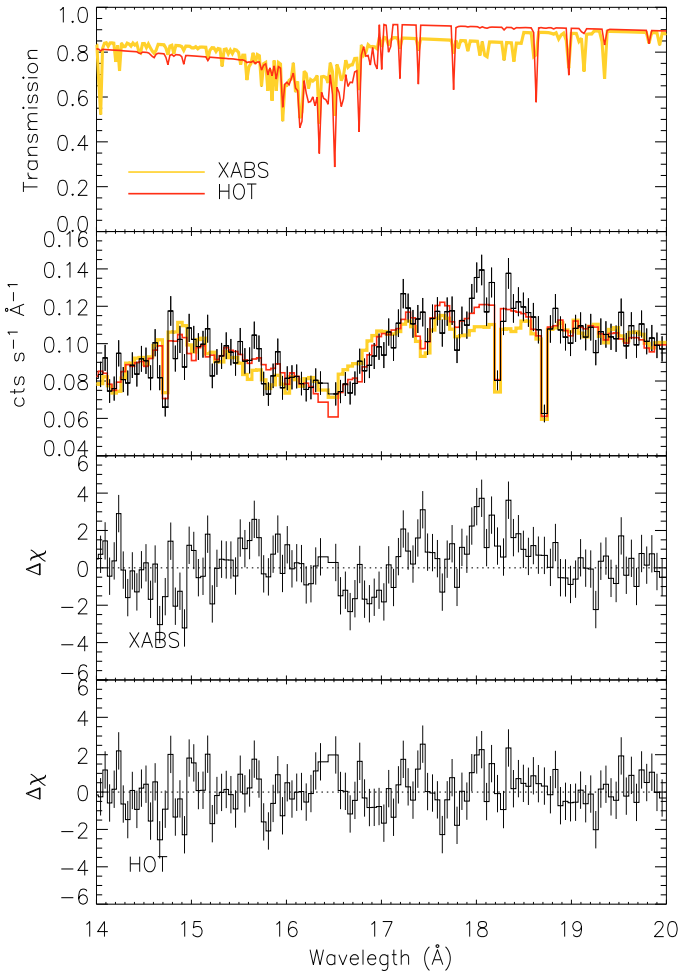

Fig. 2. Comparison between the collisionally-ionised gas model (*hot* model, dark line) and a photoionised gas (*xabs* model, light line) in the OVII edge-iron UTA wavelength region. This is a zoom of Fig. 1, *left panel*. *From top to bottom*, *first panel*: theoretical transmission curve. *Second panel*: data points together with the *hot* and *xabs* models. The *xabs* model fails to fit the data due to extra absorption by OV–OVI in the 17.5–18 Å region and in the iron UTA region. *Third and fourth panels*: residuals in terms of σ to the *xabs* and *hot* models, respectively.

photoionised absorber model causes a too shallow absorption at 16.6–17 Å. At the same time this model severely underestimates the data at 17.5–18 Å, where absorption by OVI and OVII takes place. On the contrary, the collisionally ionised absorption model provides a good fit to the data. The reason is that given a temperature, a collisionally ionised gas ionic column density distribution strongly peaks around a single ion (OVII in this case), while for a photoionised gas, a range of ions around a main ion is allowed. This produces the unwanted OV and OVI absorption in the *xabs* model in Fig. 2.

The parameters for the absorption components included in the final fit are listed in Table 2. The underlying emission is produced by a power law, a blackbody and two Gaussian to model the OVII triplet and OVIII Lyα emission lines (Table 2). The Gaussian profiles FWHM ranges from 0.25 to 0.5 Å for OVII and from 0.05 to 0.35 Å for OVIII, respectively. The main component of the OVII triplet line arises around the wavelength of the intercombination line at 21.8 Å. There is no evidence for the forbidden line at 22.1 Å. The second emission line in the fit is the OVIII Lyα line, at 18.96 Å. The value of the reduced χ^2, reported in Table 2, reflects the cross calibration uncertainties between RGS and PN that can be up to 10–15%. However we are interested in narrow features located in a spectral range where instruments are well calibrated. We verified that a slight change of the continuum shape does not affect our results.

3. Results

The persistent and the dipping state of EXO 0748–676 can be interpreted using the same model for all data groups (Table 2). While the central source flux changed over time, the continuum shape remained stable. On the contrary, the absorbers showed significant variability. In Fig. 3 we show the values of the column density of the three absorbers and the ionisation parameter of the ionised absorber as a function of time. The column density of all three absorbers systematically increases during dipping emission.

Figure 3 (first panel) shows that during dips, the column density of the neutral gas increases. As we cannot disentangle any intrinsic neutral absorber from the interstellar one, we see this as an increase of the total neutral absorption. However, the column density in the direction of the system is $\sim 1.01 \times 10^{21}$ cm^{-2} (Kalberla et al. 2005), comparable to the neutral absorber in the persistent emission. This suggests that neutral (or mildly ionised) material must exist in the vicinity of the source, in particular near the gas producing the dips.

The collisionally ionised absorber that models mainly the OVII edge (Sect. 2.2, Fig. 2) generally shows an increase in column density during dipping, while the temperature of this component does not show a clear change. The different behaviour of this ionised absorber in group A (see Table 2 and Fig. 3) is probably caused by the low statistics of that group in the dipping spectrum.

The photoionised absorber shows the same behaviour that was already found for this source by Díaz Trigo et al. (2006): during a dip the column density increases, while the ionisation parameter decreases. Compared to the persistent intervals the absorbing material becomes denser and less ionised during dips (Boirin et al. 2005).

For most groups the values of the blackbody normalisation and temperature overlap within errors when we compare dipping and persistent emission. A moderate scattering is expected due to slow changes of the persistent emission during long observations. For the power-law parameters the values of Γ and normalisation, appear instead more scattered when we compare dipping and persistent emission. This may be partially due to cross-calibration effects between RGS and PN.

4. Discussion

4.1. Evidence for a collisionally ionised gas

We find that the spectrum of EXO 0748–676 can be best modelled by adding a collisionally ionised absorber. This model well fits both the persistent and the dipping emission in all data sets. This is the first time that a collisionally ionised absorber is found in a low mass X-ray binary system. The column density of all the absorbers present in our model increases during dips suggesting an association with the gas producing the dip. A collisionally ionised plasma can exist in the presence of a high ionising radiation field ($L \sim 2 \times 10^{37}$ erg s^{-1}) only if it is located at a sufficiently large distance from the central source. If we put the gas at such a large distance ($r \sim$ few $\times 10^{11}$ cm) and we require $\xi = L/nr^2 < 1$, we find $n >$ few $\times 10^{14}$ cm^{-3}. From the measured

Table 2. Parameter values and their 1-σ errors for all data groups.

	Group A		Group B		Group C1		Group C2		Group C3	
parameter	pers	dip	pers	dip	pers	dip	pers	dip	pers	dip
neutral abs.										
$N_{\rm H}^a$	1.28 ± 0.05	3.81 ± 0.8	1.10 ± 0.03	2.21 ± 0.17	1.11 ± 0.05	2.36 ± 0.13	0.82 ± 0.02	1.48 ± 0.03	0.84 ± 0.20	1.25 ± 0.03
CI										
$N_{\rm H}^a$	4.05 ± 0.25	1.8 ± 1.6	0.95 ± 0.10	5.28 ± 0.56	$3.28^{+0.18}_{-0.40}$	5.9 ± 0.6	1.95 ± 0.07	4.1 ± 0.1	1.09 ± 0.08	3.42 ± 0.13
T^c	66 ± 3	<80	61 ± 4	63 ± 5	70 ± 3	70 ± 7	73 ± 2	69 ± 1	80 ± 4	65 ± 2
σ_v^b	<12.27	0.fixed	<4.83	123 ± 30	<7.6	<11.1	<4.7	<11.2	<3.57	<15.91
PI										
$N_{\rm H}^a$	41 ± 4	160^{+10}_{-60}	37 ± 4	74 ± 11	46 ± 4	140 ± 10	39 ± 4	80 ± 3	19 ± 2	51 ± 2
$\log\xi$	2.35 ± 0.04	2.24 ± 0.04	2.56 ± 0.04	2.36 ± 0.05	2.40 ± 0.04	2.39 ± 0.03	2.63 ± 0.04	2.38 ± 0.01	2.51 ± 0.04	2.33 ± 0.02
σ_v^b	<8.7	<6.1	<32.5	21 ± 9	<48	11^{+5}_{-8}	17 ± 2	13. ± 3	14 ± 2	11 ± 2
power law										
norm^d	1.07 ± 0.05	1.60 ± 0.16	1.80 ± 0.08	1.11 ± 0.17	1.76 ± 0.07	1.92 ± 0.12	1.85 ± 0.05	1.15 ± 0.02	1.91 ± 0.04	1.49 ± 0.04
Γ	1.23 ± 0.02	1.42 ± 0.05	1.55 ± 0.03	1.34 ± 0.08	1.42 ± 0.02	1.46 ± 0.03	1.44 ± 0.01	1.24 ± 0.02	1.47 ± 0.01	1.35 ± 0.01
blackbody										
norm^d	3.4 ± 0.5	22^{+17}_{-20}	1.20 ± 0.13	3.6 ± 1.0	1.8 ± 0.4	14. ± 6	1.10 ± 0.12	1.95 ± 0.25	1.10 ± 0.09	1.88 ± 0.21
T^c	0.10 ± 0.01	0.08 ± 0.02	0.14 ± 0.01	0.12 ± 0.01	0.11 ± 0.01	0.08 ± 0.01	0.12 ± 0.02	0.11 ± 0.01	0.12 ± 0.02	0.11 ± 0.02
O VII										
norm^e	11 ± 1	136^{+65}_{-40}	3.3 ± 0.9	27^{+13}_{-7}	9 ± 1	40 ± 8	3.6 ± 0.4	9.6 ± 0.8	2.9 ± 0.4	7.6 ± 0.7
$FWHM^f$	0.28 ± 0.04	0.35 ± 0.06	<0.5	$0.22^{+0.28}_{-0.06}$	0.23 ± 0.03	0.44 ± 0.07	0.28 ± 0.05	0.36 ± 0.05	0.24 ± 0.06	<0.5
O VIII										
norm^e	2.7 ± 0.3	16^{+14}_{-4}	$1.6^{+1.6}_{-0.4}$	$5.^{+40}_{-2}$	$2.39^{+3.74}_{-0.47}$	$8.49^{+67.96}_{-2.96}$	0.51 ± 0.16	2.32 ± 0.26	0.87 ± 0.21	1.56 ± 0.24
$FWHM^f$	0.16 ± 0.04	0.34 ± 0.09	0.07 ± 0.07	<0.11	0.07 ± 0.05	0.05 ± 0.05	$0.20^{+0.10}_{-0.08}$	$0.10^{+0.03}_{-0.02}$	0.33 ± 0.09	0.19 ± 0.05
χ^2/d.o.f.	1.29	1.41	1.42	1.52	1.38	1.50	1.68	1.83	1.59	1.66

Notes:
[a] Column densities ($N_{\rm H}$) are given in units of 10^{21} cm^{-2} for the neutral, collisionally ionised (CI) and photoionised (PI) absorbers.
[b] The width σ_v of the absorption lines is expressed in km s^{-1}.
[c] Temperatures, T, are in eV for the collisionally ionised gas and in keV for the blackbody.
[d] The normalisation (norm) of the powerlaw is given in 10^{44} ph s^{-1} keV^{-1} at 1 keV. The normalisation of the blackbody is in units of 10^{15} cm^2.
[e] The normalisation of the emission lines (OVII and OVIII) are expressed in units of 10^{42} ph s^{-1}.
[f] The FWHM of the emission lines is in Å.

column density we then derive a very narrow thickness of the gas $l = N_{\rm H}/n < 1.5 \times 10^7$ cm. The geometry of this gas could then be a uniform shell of gas, with a thickness of less than 150 km. More realistically, the medium could be inhomogeneous, with a low filling factor, as in a smoke-like medium.

In parallel, a further test of the physical process producing the absorption comes from the associated three OVII emission lines. These can be in principle used as a density/temperature diagnostic (e.g. Porquet & Dubau 2000; Cottam et al. 2001). The intercombination (x+y) line is evident in the data while due to absorption some flux from the w line may be suppressed. There is no evidence of the forbidden (z) OVII line at 22.1 Å, suggesting either a high-density photoionised gas (Cottam et al. 2001) or a collisionally ionised gas. For a photoionised gas we would also expect radiative recombination continuum of OVII, which is not detected in the data.

However, both the collisionally ionised and the $\log\xi \sim 2.5$ photoionised plasma included in our model (Table 2) do have a significant amount of OVII and OVIII and they can both contribute to the emission spectrum, making difficult to disentangle between the two ionising process contributions. The measured width of the lines is however large (Sect. 2.2). This suggests that a considerable amount of matter should be located well in the accretion disc, assuming Keplerian motion (Cottam et al. 2001). The FWHM of the detected oxygen lines is roughly 1000 km s^{-1}. Assuming a 1.4 $M_\odot$ central object then the distance must be of the order of 10^{10} cm. Therefore the emission spectrum could be dominated by the photoionised gas producing broad lines, hiding the narrow emission lines produced by the collisionally ionised gas. Indeed, the inferred line width of a collisionally ionised gas rotating at large ($r \sim$ few $\times 10^{11}$ cm) distance is of the order of 100 km s^{-1}. The absence of the OVII z line is however consistent with our requirement of $n >$ few $\times 10^{14}$ cm^{-3} for the collisionally ionised gas. For the photoionised gas, the suppression of the z line could be due either to a high gas density or to a strong UV radiation field illuminating the gas.

4.2. The geometry of the system

Here we test two simple geometries for the absorbing/emitting photoionised gas. We consider the absorption during dips as caused by photoionised gas (see Boirin et al. 2005, for full details). In both case 1 and 2, described below, we assume that the dipping gas has constant density n_d and it is located at a distance R_d from the central source in a protuberance (the impact region) of the disc.

As dips are merely caused by absorption, we further assume that the intrinsic luminosity of the source remains constant during all the observations Díaz Trigo et al. (2006) and Boirin et al. (2007).

Figure 4 depicts the geometries described in detail below. For both panels, the right hand sides describes the observer's view during the dipping state. The left hand sides shows the view during the persistent emission.

Case 1: the absorption during persistent intervals is due to a thin shell of gas of width x and ionisation parameter ξ_p (Fig. 4

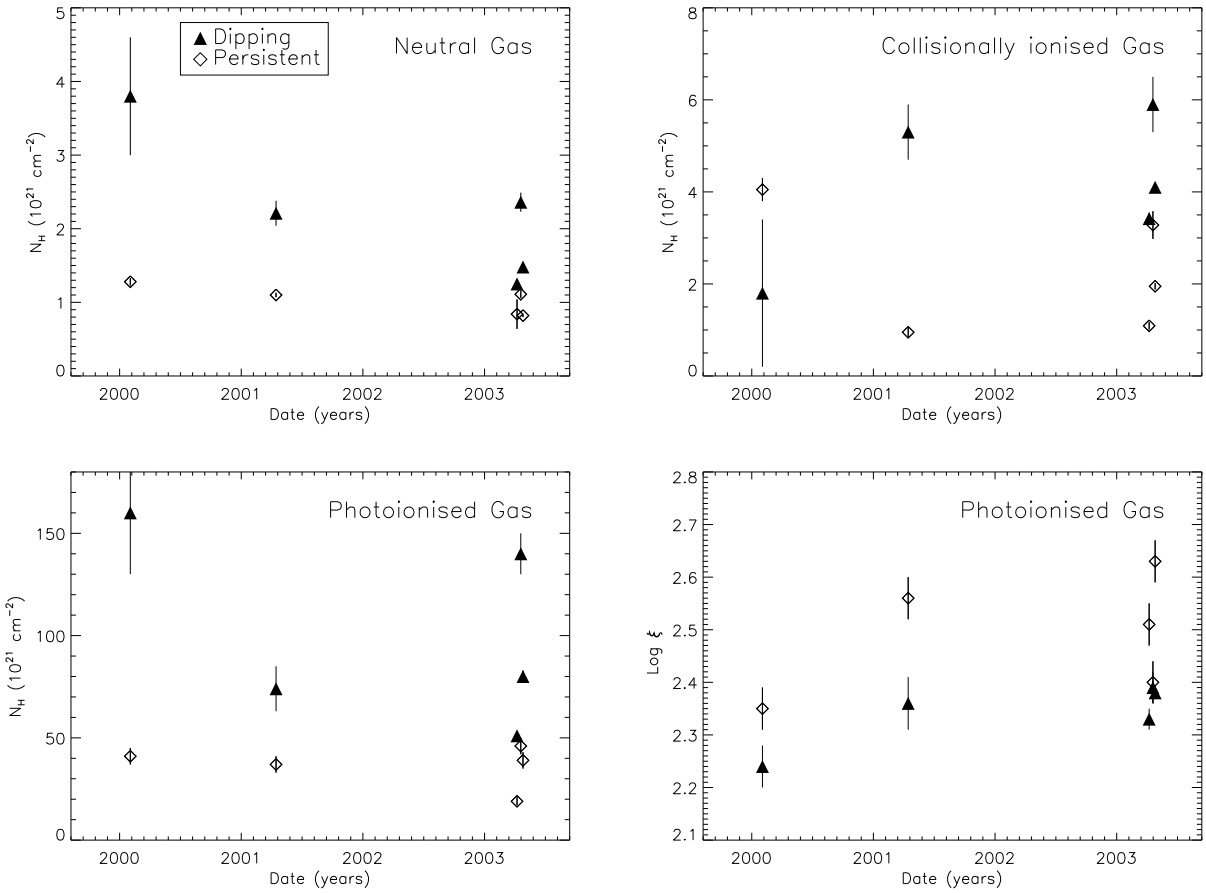

Fig. 3. Parameter values as a function of observation date. Diamonds refer to persistent and triangles to dipping state. *From top to bottom, left to right*: neutral absorber column density, collisionally ionised absorber column density, photoionised absorber column density and ionisation parameter $\log \xi$. Error bars are at 1σ level.

and the caption). The shell is located at a distance R_{p1}. We assume x to be approximately the same as the size of the compact impact region that produces the dips (Fig. 4, upper-right panel). The rationale behind this is that the gas that produces the persistent absorption could well be gas that trails from the impact region into the rest of the disc. With the assumption that the intrinsic luminosity does not depend on the dipping state of the source, we can compute:

$$\frac{\xi_d}{\xi_p} = \frac{n_p R_{p1}^2}{n_d R_{d1}^2} \tag{1}$$

where ξ is the ionisation parameter defined before, n the hydrogen density, R the distance to the ionising source and the subscripts p and d refer to persistent and dipping emission respectively.

Since we assume that the density has no radial dependence, we can rewrite the above for case 1 as:

$$\frac{R_{p1}}{R_{d1}} = \sqrt{\frac{\xi_d \cdot N_{\mathrm{H},d}}{\xi_p \cdot N_{\mathrm{H},p}}}. \tag{2}$$

Here $N_{\mathrm{H}} = xn$ is the hydrogen column density derived from our fits for the dipping ($N_{H,d}$) and persistent ($N_{H,p}$) emission (see Sect. 3 and Table 2).

Case 2: the persistent gas is in a spherical cloud encompassing the whole neutron-star-disc system (lower plot in Fig. 4). This cloud of photoionised gas with ionisation parameter ξ_p has a radius R_{p2} a density n_p. The dipping gas is again a compact region of width x (Fig. 4, lower-right panel). In this second case we further make the assumption that the disc is geometrically thin (Frank et al. 2002; Lewin et al. 1995). Therefore, we consider the height of the disc $H \sim 0.1R_{d2}$ and also $H \sim x$ (Fig. 4).

The persistent gas is sphere-shaped, therefore $N_{\mathrm{H},p} = R_{p2}n_p$. For the dipping gas $N_{\mathrm{H,d}} = xn_d = Hn_d = 0.1R_{d2}n_d$, because of the simple relation between H and R_{d2} defined above. We can now substitute the values of N_{H} in Eq. (1) and obtain the relation between R_p and R_d for case 2:

$$\frac{R_{p2}}{R_{d2}} = \frac{10 \cdot \xi_d \cdot N_{\mathrm{H},d}}{\xi_p \cdot N_{\mathrm{H},p}}. \tag{3}$$

For both case 1 and case 2, we have calculated the value of R_p/R_d and listed them in Table 3. The values for N_{H} and ξ are taken from Table 2.

We see that in case 1 the radius of the shell is comparable to the distance of the impact region to the central source ($R_d \approx R_p$). This is consistent with the idea that the shell could be a continuation of the impact region. On the contrary, in case 2 the cloud of gas in the persistent state is an order of magnitude larger ($R_p \gg R_d$) than the distance of the impact region to the central source.

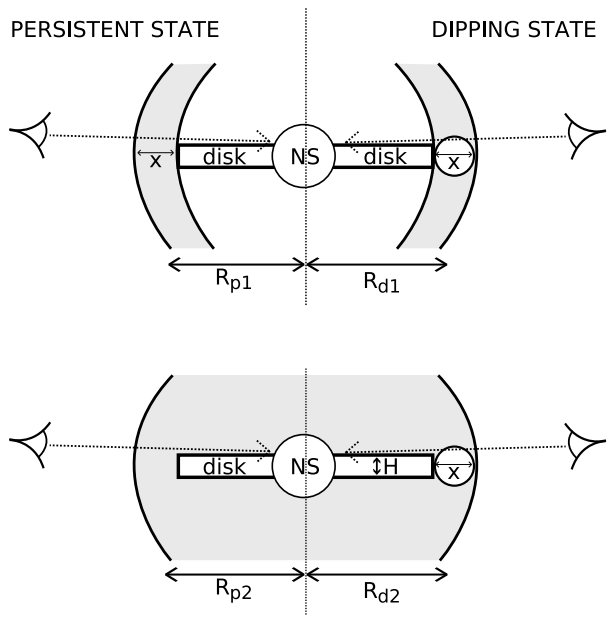

Fig. 4. Two possible geometries: case 1 in the upper plot the gas producing the persistent absorption has a shell-like geometry of thickness x and distance R_{d1} from the central source. In case two (*lower plot*) the persistent gas is a cloud-like geometry of radius R_{p2} encompassing the whole system. The labels "NS" and "disc" indicate the position of the NS and the accretion disc, respectively. On the right-hand side of the drawings, on both panels, is the impact region of size x and distance R_d from the central source. The drawn line of sights indicates which environments the observer intercept during the persistent and dipping state.

4.3. A flattened geometry for the persistent gas

For both case 1 and 2 described in the previous section, it is also possible to put additional constraints on the geometry of the persistent absorbing gas. This can be achieved using the OVII and OVIII emission lines and the absorption edges (Cottam et al. 2001). As justified in Sect. 4.1, we assume here that the emission lines are dominated by photoionisation. In this calculation we only use the OVII line and edge for the data groups where the associated errors on those values were the smallest. Therefore we excluded group B.

We start with the equation for the line luminosity of a given ion i (Liedahl 1999):

$$L^i_{\rm line} = \int n_{\rm e}^2 {\rm d}V \alpha_{\rm RR}(T)\eta_l f_z A \quad [{\rm ph/s}], \tag{4}$$

where $n_{\rm e}$ is the electron density, $\alpha_{\rm RR}$ is the radiative recombination coefficient for the transition, η_l is the fraction of recombinations that produce the line, f_z is the fractional abundance of the ion in ionisation state $i+1$ and A is the absolute abundance of the element. The radiative recombination coefficient $\alpha_{\rm RR}$ at 10 eV, which corresponds to the plasma temperature for the best-fit ionisation parameter, is $\alpha_{\rm RR(OVII)} = 1.6 \times 10^{-11}\,{\rm cm^3\,s^{-1}}$ (Verner & Ferland 1996). The fraction of recombinations that produce the OVII line is $\eta_{l({\rm OVII})} = 0.75$ (Cottam et al. 2001). The absolute abundance for oxygen is taken from Anders & Grevesse (1989): $A = 8.5114 \times 10^{-4}$. The emission measure is defined as:

$$EM = \int n_{\rm e}^2 {\rm d}V = \frac{L_{\rm line}}{\alpha_{\rm RR}(T)\eta_l f_z A}\,. \tag{5}$$

Table 3. The ratio of the persistent over dipping radius R_p/R_d for the two geometries and for each data group (A–C3).

	A	B	C1	C2	C3
case 1	1.7 ± 0.4	1.1 ± 0.1	1.7 ± 0.2	1.1 ± 0.1	1.3 ± 0.1
case 2	30 ± 13	13 ± 3	30 ± 6	11 ± 2	17 ± 3

Table 4. Observed and calculated values to obtain relevant geometrical and physical parameters of the photoionised gas (Sect. 4.3, 4.4).

		A	C1	C2	C3
observed values					
$L_{\rm cont}$	10^{37} ergs/s	1.38	1.05	1.06	0.97
$\log\xi$	erg cm	2.35	2.40	2.63	2.51
$N_{\rm H}^{\rm xabs}$	10^{22} cm^{-2}	4.12	4.63	3.97	1.94
f_z		0.317	0.274	0.132	0.200
$L_{\rm line}$	10^{42} ph/s	11.2	9.04	3.63	2.97
calculated values					
EM	10^{57} ph/cm^3	3.46	3.23	2.69	1.45
nr^2	10^{34} cm^{-1}	6.16	4.18	2.48	3.00
case 1					
nx	10^{22} cm^{-2}	0.45	0.62	0.86	0.39
$f' = N_{\rm H}^{\rm xabs}/(nx)$		9.23	7.47	4.62	4.97
n	10^{11} cm^{-3}	27.6	50.4	64.0	12.2
R_p	10^{11} cm	1.4	0.9	0.6	1.5
R_d	10^{11} cm	0.8	0.5	0.5	1.1
M	10^{-12} $M_\odot$	1.1	0.5	0.2	0.6
case 2					
nr	10^{22} cm^{-2}	1.34	1.85	2.59	1.16
$f' = N_{\rm H}^{\rm xabs}/(nr)$		3.08	2.50	1.53	1.67
n	10^{11} cm^{-3}	0.2	0.5	0.6	0.1
R_p	10^{11} cm	14.9	9.0	6.2	15.5
R_d	10^{11} cm	0.5	0.3	0.5	0.9
M	10^{-12} $M_\odot$	22.5	8.9	3.1	10.9

The integral in Eq. (5) can be estimated for both the shell-like (case 1) and the sphere-like (case 2) geometry for the persistent gas.

For case 1, for a shell extending from r to $r + x$ ($x \ll r$) we have

$$nx = \frac{EM_{\rm shell}}{4\pi nr^2}\,. \tag{6}$$

In fact we consider $r \equiv R_p$. For case 2 we simply have for a sphere of gas:

$$nr = \frac{3}{4\pi}\frac{EM_{\rm sphere}}{nr^2}\,. \tag{7}$$

The value of nr^2 can be derived from the ionisation parameter:

$$nr^2 = \frac{L_{\rm cont}}{\xi}\,. \tag{8}$$

Inserting Eq. (8), the column densities of Eqs. (6) and (7) are now a function of the ionised absorber, the line luminosity, the emission measure and the photoionisation parameter. All these parameters can be evaluated from the spectral analysis.

In Table 4 we compare the expected column density (for case 1, nx and case 2, nr) of the gas, as derived by the line emission, with the one we measure (from the absorbed spectrum) for each data group.

Assuming at first that the material subtends a solid angle (as seen from the neutron star) of 4π sr, the emission of the

line will be maximised and, as a consequence, also the derived column density of the photoionised emitting gas. If we attribute any difference to geometrical effects, the ratio between observed/expected column density provides us a flattening factor (Table 4). From the table we see that the derived column density is systematically lower than the measured one, suggesting that the material does not fully extended in the vertical direction, but rather it is flattened.

In case 1 the flattening factor f' is ~4.5–9. In case 2 the discrepancy between observed and expected column density is somewhat lower, ~1.5–3. For case 1, the flattening factor is in agreement with that found previously for this source (Cottam et al. 2001). Converting the flattening factor into an opening angle, the ionised persistent gas subtends an average angle of 18° for case 1 and a wider angle of 54° for case 2.

4.4. Density, size, and mass of the photoionised gas

Using the information we gathered above, we calculated the values for the gas density n and distance R_p (Table 4). For both geometries we use the identity: $n = (nr)^2/nr^2$.

For case 1 we adopt $x \approx 0.1 \times r$ as the thickness of the shell. We obtain:

$$n = 100\frac{(nxf')^2}{nr^2} = \left(\frac{10f'L_{\rm line}}{4\pi\alpha_{\rm RR}\eta f_z A}\right)^2\left(\frac{\xi}{L_{\rm cont}}\right)^3,$$
$$r \equiv R_p = 0.1\frac{nr^2}{nxf'} = \frac{0.4\pi\alpha_{\rm RR}\eta f_z A}{f'L_{\rm line}}\left(\frac{L_{\rm cont}}{\xi}\right)^2. \quad (9)$$

For case 2 we have:

$$n = \frac{(nrf')^2}{nr^2} = \left(\frac{3f'L_{\rm line}}{4\pi\alpha_{\rm RR}\eta f_z A}\right)^2\left(\frac{\xi}{L_{\rm cont}}\right)^3,$$
$$r \equiv R_p = \frac{nr^2}{nrf'} = \frac{4\pi\alpha_{\rm RR}\eta f_z A}{3f'L_{\rm line}}\left(\frac{L_{\rm cont}}{\xi}\right)^2. \quad (10)$$

The average distance from the neutron star to the dipping material R_d is simply obtained using the R_p/R_d ratio (Table 3). The distance from the neutron star to the inner Lagrangian point (L1) varies between 6.4–9.7 × 10^{10} cm (Frank et al. 2002). For both the geometries under study, the location of the dipping material, where the flow of matter from the donor impinges into the accretion disc, is consistent with the distance of L1. The gas seen during the persistent phase is at approximately the same distance of the dipping point in case 1, while in case 2 the sphere of persistent gas should extend much further. The average thermal velocity of the photoionised gas ($v_{\rm therm} \sim 77\,{\rm km\,s^{-1}}$) is more than a factor two lower than the escape velocity at a distance of 10^{12} cm ($v_{\rm esc} \sim 190\,{\rm km\,s^{-1}}$). Therefore in principle the photoionised gas can survive also beyond L1.

Observational evidence of cold gas extending beyond the orbits of the components has been found in infra-red for different types of binary systems (e.g. cataclysmic variables, novae etc., Deufel et al. 1999; Solheim & Sion 1994), including neutron stars (Muno & Mauerhan 2006). The existence of such material, leading possibly to the formation of a circumbinary disc (Dubus et al. 2002), would have important implications for the evolutions of the binary system (Spruit & Taam 2001). In this scenario, the detected collisionally ionised gas (Sect. 4.1) could also be a further extension, too far away to be photoionised, of the persistent emission. However, the measured temperature of the collisionally ionised gas is ~70 eV, which translates in a thermal velocity $v_{\rm therm}$ of about 140 km s^{-1}. If the gas is located at a distance $\gtrsim 10^{12}$ cm from the central source $v_{\rm therm}$ becomes comparable to the escape velocity $v_{\rm esc} \sim 190\,{\rm km\,s^{-1}}$, making the gas a short-lived component, unless continuously replenished by the accretion disc activity. However, if the distance is ~10^{11} cm, the escape velocity already becomes four times larger than $v_{\rm therm}$, guaranteeing the stability of the collisionally ionised gas. This would favour a scenario similar to case 1, where the distance of the persistent and dipping gasses range between 0.5 and 1.4 × 10^{11} cm. With this geometry, the collisionally ionised gas could well be an extension of the persistent gas, perhaps constituting a first, hotter, portion of a circumbinary disc, which may eventually join a colder phase ($T \sim 600$ K) which extends up to four times the distance of the accretion disc (Muno & Mauerhan 2006).

In the hypothesis that the collisionally ionised gas is at a distance comparable to the persistent and dipping material, it is likely that there is interaction with the system where the accretion stream impacts with the disc, together with neutral material. A higher concentration (implying a higher column density) of the collisionally ionised and neutral gas in correspondence with the dipping material is then possible (e.g. Boirin et al. 2005, and Sect. 3).

The average gas density is of the order of few × 10^{12} cm^{-3} for a shell-like geometry (case 1, Table 4) and about 100 times less for the spherical geometry (case 2, Table 4). However, the complete suppression of the forbidden line in the persistent spectrum requires a gas density >10^{14} cm^{-3}, unless the gas is irradiated by a strong ultraviolet field. Therefore, if the shape of the OVII triplet is dominated by density effects, we have to require that n is not uniform in the gas, having for example a radial gradient.

Finally, we calculate the mass of the persistent gas enclosed both in a flattened shell and in a sphere using $M = nm_pV$ where M is the mass in the gas, n is the density, m_p is the proton mass and V is the volume of the gas (Table 4).

5. Conclusions

In this paper we present the spectral analysis of a large *XMM-Newton* data set of EXO 0748–676 mainly focusing on the RGS high-energy resolution data in order to investigate in depth the gaseous environment of the source.

For both the persistent and dipping spectra, the best fit model is a combination of a neutral absorber, a collisionally ionised absorber, a photoionised absorber, a power law, a black body and two Gaussian emission lines at the energies of OVII intercombination line and the OVIII Ly α. The scatter in the parameter values for the different data groups gives an idea of the level of uncertainty of our conclusions.

Here we summarise the main physical implications of this analysis:

- The gas during the dipping phase has a higher column density and it is less ionised than the gas in the cloud that permanently surrounds the system.
  This is in line with the idea of ionised absorbers causing the dipping phenomenon (Boirin et al. 2005; Díaz Trigo et al. 2006). In this scenario the compact and colder impact region, where the accretion stream hits the disc, is in our line of sight during dipping intervals.
- We used the information obtained from the RGS spectral analysis to investigate the geometry of the persistent/dipping gas and their distance from the central source.
  First, in the hypothesis of the persistent gas in a shell form, we obtain that the thickness and the radius (~few × 10^{11} cm)

of the shell are consistent with those of the dipping gas. The intuitive picture is that the persistent gas is a trailing tail of the dipping gas. This axial symmetric geometry should be flattened with an opening angle of roughly 18°, consistently with previous studies of this source (Cottam et al. 2001).

In a second scenario, where a spherical cloud of persistent gas was considered, we find a smaller flattening, as the angle subtended by the gas is ~54°. The persistent gas extends about ten times further than the distance of the dipping gas. The radius of the gas sphere is about $0.9–1.5 \times 10^{12}$ cm, i.e. larger than the first Lagrangian point. Photoionised material at such a distance might be the first portion of a wider circumbinary disc, detected in infra red in at least two neutron stars systems (Muno & Mauerhan 2006).

For both geometries the gas density is not sufficiently high to justify the suppression of the OVII forbidden line in favour of the OVII intercombination line (Porquet & Dubau 2000). However, assuming that the emission line is broadened by Keplerian motion around the central source, we infer a lower limit for the location of the emitting gas of $\sim 10^{10}$ cm, implying a higher gas density ($\sim 10^{14}$ cm^{-3}). This value is certainly sufficient to produce the observed OVII triplet ratios (Porquet & Dubau 2000). This suggests that there may be a radial dependence of the gas density. Another possibility is that the forbidden line in the photoionised gas is suppressed by a strong UV field.

– It is the first time that a collisionally ionised absorber is found in a low mass X-ray binary system. In order for this component to survive to the strong radiation field, it should be located far away from the central source ($r \sim$ few $\times 10^{11}$ cm). This is supported by the evidence that both the temperature and the column density of such gas change very little during the dipping or persistent phase and seem to be unperturbed on very long (years) time scale. We estimated that this collisionally ionised absorber should be in the form of dense filaments, with a very low filling factor. In the hypothesis of a circumbinary disc, this gas might also be an ulterior continuation of the persistent gas. In this case the collisionally ionised gas should not be located beyond few $\times 10^{11}$ cm, in order not to easily escape the system. This would favour a more compact-sized geometry for the whole gas environment of the neutron star, as the one described in case 1, where the persistent gas is a trailing tail of the dipping bulge, at a distance of about 10^{11} cm.

Acknowledgements. The authors wish to thank the anonymous referee for his/her useful comments. The Space Research Organisation of the Netherlands is financially supported by NWO, The Netherlands Organisation for Scientific Research.

References

Anders, E., & Grevesse, N. 1989, Geochim. Cosmochim. Acta, 53, 197
Boirin, L., Méndez, M., Díaz Trigo, M., Parmar, A. N., & Kaastra, J. S. 2005, A&A, 436, 195
Boirin, L., Keek, L., Méndez, M., et al. 2007, A&A, 465, 559
Bonnet-Bidaud, J. M., Haberl, F., Ferrando, P., Bennie, P. J., & Kendziorra, E. 2001, A&A, 365, L282
Church, M. J., Balucinska-Church, M., Dotani, T., & Asai, K. 1998, ApJ, 504, 516
Cottam, J., Kahn, S. M., Brinkman, A. C., den Herder, J. W., & Erd, C. 2001, A&A, 365, L277
Cottam, J., Paerels, F., & Mendez, M. 2002, Nature, 420, 51
den Herder, J. W., Brinkman, A. C., Kahn, S. M., et al. 2001, A&A, 365, L7
Deufel, B., Barwig, H., Šimić, D., Wolf, S., & Drory, N. 1999, A&A, 343, 455
Díaz Trigo, M., Parmar, A. N., Boirin, L., Méndez, M., & Kaastra, J. S. 2006, A&A, 445, 179
Dubus, G., Taam, R. E., & Spruit, H. C. 2002, ApJ, 569, 395
Frank, J., King, A., & Raine, D. 2002, Accretion power in astrophysics, 3rd Ed. (Cambridge University Press), 384
Frank, J., King, A. R., & Lasota, J.-P. 1987, A&A, 178, 137
Gottwald, M., Haberl, F., Parmar, A. N., & White, N. E. 1986, ApJ, 308, 213
Hertz, P., Wood, K. S., & Cominsky, L. 1995, ApJ, 438, 385
Hertz, P., Wood, K. S., & Cominsky, L. R. 1997, ApJ, 486, 1000
Homan, J., Wijnands, R., & van den Berg, M. 2003, A&A, 412, 799
Jimenez-Garate, M. A., Schulz, N. S., & Marshall, H. L. 2003, ApJ, 590, 432
Kaastra, J. S., Mewe, R., & Nieuwenhuijzen, H. 1996, in UV and X-ray Spectroscopy of Astrophysical and Laboratory Plasmas, 411
Kalberla, P. M. W., Burton, W. B., Hartmann, D., et al. 2005, A&A, 440, 775
Lewin, W. H. G., Van Paradijs, J., & Van den Heuvel, E. P. J. 1995, X-ray binaries (Cambridge University Press), 662
Liedahl, D. A. 1999, in Lecture Notes in Physics, X-Ray Spectroscopy in Astrophysics, ed. J. van Paradijs, & J. A. M. Bleeker (Berlin Springer Verlag), 520, 189
Muno, M. P., & Mauerhan, J. 2006, ApJ, 648, L135
Parmar, A. N., Smale, A. P., Verbunt, F., & Corbet, R. H. D. 1991, ApJ, 366, 253
Parmar, A. N., White, N. E., Giommi, P., & Gottwald, M. 1986, ApJ, 308, 199
Porquet, D., & Dubau, J. 2000, A&AS, 143, 495
Sidoli, L., Parmar, A. N., & Oosterbroek, T. 2005, A&A, 429, 291
Solheim, J.-E., & Sion, E. M. 1994, A&A, 287, 503
Spruit, H. C., & Taam, R. E. 2001, ApJ, 548, 900
Strüder, L., Briel, U., Dennerl, K., et al. 2001, A&A, 365, L18
Thomas, B., Corbet, R., Smale, A. P., Asai, K., & Dotani, T. 1997, ApJ, 480, L21
Turner, M. J. L., Abbey, A., Arnaud, M., et al. 2001, A&A, 365, L27
Verner, D. A., & Ferland, G. J. 1996, ApJS, 103, 467
White, N. E., & Swank, J. H. 1982, ApJ, 253, L61
Wolff, M. T., Becker, P. A., Ray, P. S., & Wood, K. S. 2005, ApJ, 632, 1099